Nanosecond time-resolved multiprobe imaging of laser damage in transparent solids

H. Jiang, J. McNary, and H. W. K. Tom[a)]
Department of Physics, University of California, Riverside, Riverside, California 92521

M. Yan, H. B. Radousky, and S. G. Demos
Lawrence Livermore National Laboratory, Livermore, California 94551

(Received 18 February 2002; accepted 9 August 2002)

We report the nanosecond time-scale and micron length-scale dynamics of elastic wave, plastic deformation, melt-front and crack propagation during laser-induced damage in the bulk of an optically transparent crystalline solid. Time-delayed probe pulses with wavelengths corresponding to RGB-color filters are used to obtain multiple images during a single damage event. This technique enables ''real-time'' dynamical studies of complex transient phenomena. © *2002 American Institute of Physics.* [DOI: 10.1063/1.1511536]

We report the ns time-resolved and μm spatially resolved dynamics of material failure accompanying pulsed-laser-induced damage of the nonlinear optical material KD_2PO_4 (DKDP). Using a color-multiplexing optical imaging scheme, we obtain multiple ns time-delayed images during a single laser-induced event. By obtaining ''real-time'' information we avoid the shot-to-shot variations in both the load and morphological evolution that have complicated laser damage studies in the past. Mechanical and pulsed-laser driven shock have been studied in planar geometry with ps time-resolved Raman spectroscopy[1,2] and time-resolved interferometric imaging.[3] Crack dynamics has been studied experimentally under quasistatic load.[4,5] Planar melt-front dynamics driven by fs lasers has been time resolved in semiconductors.[6] Ns time-resolved x-ray diffraction[7] and holography[8] have also been developed. Here, we report the observation of strain, plastic deformation, melt front, and fracture under divergent rather than planar load.

The experimental setup is shown schematically in Fig. 1. The 15 ns full width at half maximum (FWHM) duration pump pulse was derived from the 1.064 μm wavelength output from a diode-laser injection-seeded Q-switched Nd:YAG laser. The central Airy ring obtained after pinhole spatial-filtering was focused into the bulk of a DKDP crystal with a nearly Gaussian profile with waist $w_0=29$ μm. Three probe pulses were derived from the second-harmonic (SH) output of the same laser by stimulated Raman scattering in a 1 m cell of CH_4 gas at 4 atm. The 5 ns Stokes (629.7 nm), 10 ns SH (532 nm), and 3 ns anti-Stokes (460.6 nm) pulses coincide with the red, green, and blue filter spectra of the camera. The three probe beams were spatially filtered, dispersed with a prism, adjusted in amplitude with filters, and time delayed with respect to the pump by propagation in free space. The beams were recombined in a dispersing prism and passed unfocused at 90° through the focal region of the pump. The interaction region was imaged in transmission into a 1/3 in. color three-element charge coupled device (3-CCD) camera (Panasonic GP-US502) using a long working distance 20× microscope objective. The camera disperses the RGB probe beams onto three spatially registered CCD's. The DKDP crystals were grown by a rapid-growth technique at Lawrence Livermore National Laboratory (LLNL).[9] The peak incident pump laser fluence on focus was 68–80 J/cm^2 and damaged with 20%–60% probability, respectively. This is consistent with bulk damage threshold measurements performed at LLNL on the highest-quality material. $1\times1\times1$ cm^3 samples were oriented along $x-y-z$ principal axes and six sides were optically polished and diamond turned at LLNL. The absorbed pump laser intensity was measured by detecting the transmitted power with 300 ps resolution. Absorption onset occurred at the peak intensity of the pump pulse ($t=0$) consistent with breakdown by multiphoton absorption. The pump energy was deposited in a ~7.5 ns FWHM pulse. RGB images at the same time delays showed that the size and spatial orientation of image features did not depend on probe wavelength.

Images in Fig. 2, rows (a)–(d), show four laser-induced damage events with 1.2 mJ incident pump energy and 0.1, 0.2, 0.4, and 0.6 mJ absorbed energy, respectively. For each event, the first three time-sequenced images were obtained using the ns time-delayed RGB probe pulses and the fourth image was taken 2 s after the pump using the blue probe. The pixel resolution was 1.23×1.23 μm^2 at the interaction image plane. The images were obtained through crossed linear polarizers (P and A in Fig. 1) set along $x=[100]$ and $y=[010]$,

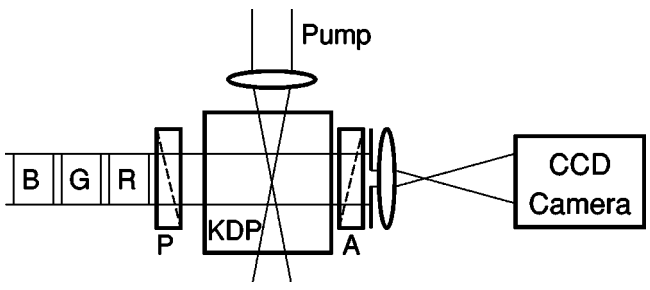

FIG. 1. Schematic of experimental optical arrangement. Time-delayed R, G, and B probe pulses back illuminate the interaction region pumped along the focal plane of the imaging CCD camera. A pair of prism polarizers can be used to polarize (P) and analyze (A) the polarization of the probe.

a)Electronic mail: harry.tom@ucr.edu

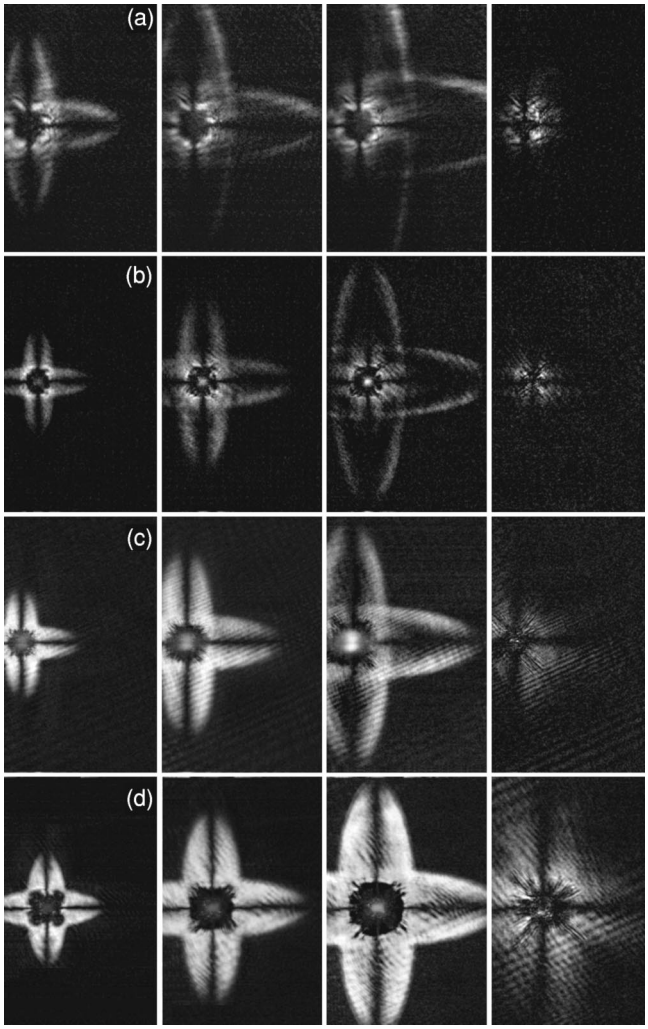

FIG. 2. Time-resolved images of laser-induced damage viewed in $x-y$ plane. Rows (a)–(d) show 4 events with 0.1, 0.2, 0.4, and 0.6 mJ absorbed laser fluence, respectively. From the left- to the right-hand side, row (a) images taken at 40 ns, 60 ns, 80 ns, and 2 s delay. Rows (b)–(d) images taken at 20 ns, 35 ns, 50 ns, and 2 s delay. Images are 355×588 μm^2.

the horizontal and vertical axes of Fig. 1, respectively. The probe was incident along the $z=[001]$ axis. DKDP is a uniaxial crystal. In this geometry, the crossed-polarized image is normally dark without strain. The bright image intensity is due to the path-integrated birefringence along the z direction. By symmetry, the image is always dark along the x and y directions.[10] The pump was incident along x.

Even with the probe beams blocked, we observed the small bright spot in the dark central region due to emission from the laser-heated plasma at the damage nucleation site. The spectrally integrated emission intensity had a 10 ns FWHM peaked at $\sim$5 ns delay time. Outside the pump waist w_0, and at times $>$10 ns, all birefringence is due to strain as field-induced birefringence is negligible.

The leading edge of the outgoing strain wave forms a crossed double-ellipse pattern in the $z=0$ plane. A comparison of Figs. 2(b)–2(d), and events at other time delays, allows us to conclude that the leading edge velocity was independent of the absorbed pump energy, constant for time delays $>$10 ns, and fit both the anisotropic shape and velocity expected for elastic wave propagation with a point disturbance using the room temperature and 1 atm DKDP elastic

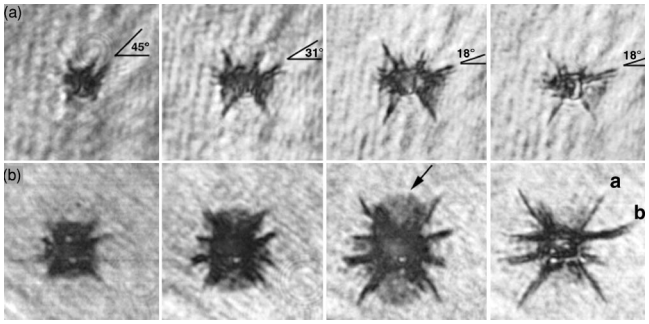

FIG. 3. Time-resolved images of laser-induced damage viewed in $x-z$ plane. Rows (a) and (b) show damage with 0.2 and 0.4 mJ absorbed laser fluence. Left- to right-hand side images taken at 20 ns, 35 ns, 50 ns, and 2 s delay, respectively. Images are 250×250 μm^2.

constants.[10] The expected velocities of the x polarized (fast) and y polarized (slow) wave along [100] are $\sqrt{c_{11}/\rho}=5.37$ km/s and $\sqrt{c_{66}/\rho}=1.59$ km/s, respectively. The coherent superposition of those wave fronts produce a quasilongitudinal displacement along [110] traveling at 2.16 km/s. The longitudinal wave speed along [001] is expected to be $\sqrt{c_{33}/\rho}=4.83$ km/s. The measured wave speeds were: 5.35 $\pm$0.05, 1.60$\pm$0.05, 2.15$\pm$0.05, and 4.8$\pm$0.2 km/s, respectively, in excellent agreement. In an event with absorbed pump fluence similar to Fig. 2(b), we used a birefringence-calibrated image and a numerical simulation of the path-integrated birefringence through an error-function-shaped leading edge to estimate the peak amplitude and gradient to be 0.5 GPa and 0.09 GPa/μm at 50 ns delay. Because the strain waves propagate at the calculated values, we can use these magnitude values to calculate the strain and strain gradients back to 10 ns time delay and find 12.5 GPa and 2.25 GPa/μm, respectively. Amplitudes would be higher in events of Figs. 2(c) and 2(d).

With an absorbed pump fluence similar to that shown in Fig. 2(c), the average velocity of the longitudinal wave along [100] between 0 and 10 ns was 5.6$\pm$0.1 km/s which is higher than the elastic speed by more than our error bar. The leading edge propagates as a shock wave but only at times $<$10 ns.

The dark circular feature centered at the damage nucleation site in Fig. 2 appears dark with very high contrast. In Fig. 3, we show images obtained in the same laser geometry but with the crystal rotated with $x=[100]$ and $z=[001]$ axes in the horizontal and vertical directions, the probe beam incident along the $y=[010]$ axis, and no crossed linear polarizers in the probe beam. The absorbed pump energies in Figs. 3(a) and 3(b) were 0.2 and 0.4 mJ out of 1.2 mJ incident pump energy, respectively. In Fig. 3(a) at 50 ns, the dark region is anisotropic with the $x-z$ ratio$=$1.4. In Fig. 3, image contrast is due only to scatter, refraction (lensing), or absorption and a large index difference is required to produce the observed $>$95% contrast. For pure refraction, lensing at object sizes up to the $\sim$50 μm radius in Fig. 2(d), would require the average refractive index $n>3$. The average edge of the dark region is quite sharp in the object plane with a 90% to 10% fall off of 2.5$\pm$0.5 μm (near pixel resolution). Such a large and spatially sharp refractive index gradient ($n=1.5$ in the surrounding material) implies a phase front. At 35 ns in Fig. 2(d), the upper bound on the average temperature in the ''dark'' volume is 900 °C assuming the total ab-

sorbed energy is distributed in the ellipsoidal volume ($r_{x,y}$=48 μm, r_z=34 μm) and the heat capacity is that of the room-temperature crystal. If the dark region were still in that state with an 8 eV band gap, the thermalized plasma density would be negligible. The energy density is, however, high enough for solid–solid and melting phase transitions. The equilibrium melt temperature[11] is 430 °C at 4 GPa with a transition line slope of 50 K/GPa so the melt is energetically accessible under the experimental conditions of 12 GPa, >830 °C at 10 ns delay and marginally accessible at longer delays when the dark region stops expanding.

We identify the phase as a liquid because the sign of the birefringence tells us the strain wave is compressive and only the melting transition is volume expanding while all known solid–solid transitions in DKDP/KDP[11,12] are either volume continuous or contracting. The bright region between the dark circle and leading edge of the strain wave in Fig. 2 is also due to compressive strain. Assuming the strain propagates outward at the 300 K speed of sound, then in Figs. 2(b)–2(d) the driving strain pulses are 27, 40, and >50 ns in duration, respectively. The dark region stops growing between 20–35, 35–50, and after 50 ns. This temporal correlation implies the strain is due to the continued compression of material as the phase-front advances. In addition, cracks are ''annihilated'' as the phase boundary grows to incorporate them. This is seen in Fig. 3: The tail of a crack initially propagating at 45° and then at 31° is obscured inside the phase boundary as it grows and the crack tip at 18° appears to have been the template for the crack to regrow into the center as the dark region contracts upon cooling. This is consistent with melting and resolidification.

These arguments together allow us to deduce that we have imaged melt-front propagation. In the $x-y$ plane it is radially symmetric with an average melt-front velocity of 0.80 and 1.0 km/s between 20–35 ns in Figs. 2(c) and 2(d), respectively, and 0.88 km/s between 35–50 ns in Fig. 2(d). These speeds are 50%–60% of the slowest sound velocities in the $x-y$ plane. The $x-z$ anisotropy is 1.4($\pm$0.05):1. The thermal conductivity in the tetragonal solid is nearly isotropic. However, at constant volume, a spherical thermal gradient generates 2.8 times more pressure in the z direction. The linear thermal expansion coefficient is 2 times higher in z than in the $x-y$ plane and the fractional linear compressibility is 1.4 times lower. This pressure anisotropy suppresses the melt front in z relative to the $x-y$ direction.

The strain remaining 2 s after the pump (fourth column) is due to plastic deformation. In Figs. 2(a) and 2(b) there are no significant changes in the μm-scale plastic deformation after the falling edge of the outward propagating strain wave, i.e., deformation occurs during expansion of the melt rather than during resolidification. DKDP is a ductile material. The observation in Fig. 2(a) that deformation occurs in the absence of cracking shows directly that the threshold conditions for plastic deformation remain lower than the threshold for cracking even on the ns time scale.

Two types of cracks were observed, both propagating in the [110]–z plane. Type *a* cracks (marked *a* in Fig. 3) propagate in a single direction outward from the melt front in the equivalent [1,1,1.65($\pm$0.1)] directions. The average velocities of type *a* cracks range from 1.4 to 2.1 km/s between 20 and 35 ns delay. On average, type *a* cracks propagate faster and for longer distances than type *b*. Type *b* cracks appear in the equivalent [1,1,β] directions where β decreases during the damage event from initial values as high as 1 to final values of 0.3 to 0.13. In Fig. 3(a), a type *b* crack changes propagation direction from 45° to 18° in the $x-z$ projected plane between 20 and 50 ns delay. A curved track is not observed because the back end of the crack is obscured by the advancing melt front. The observation that the direction always shifts toward lower β, which also is the direction of slower strain wave speed, suggests that the crack tip may be guided dynamically in the direction where crack speed is a constant fraction of strain wave speed.

In the event of Fig. 3(b) (see arrow), an additional ellipsoidal optical feature appears brighter than the liquid but darker than the initial solid phase. It expands in the z direction after 20 ns but is confined to the melt-front diameter along x. Because of the significant image contrast and abrupt difference in index of refraction, we assign this feature to a high-pressure ordered solid phase. Observation of cracks in this region rules out the possibility of it being a liquid. It is probably an ordered phase because the after-damage optical transparency of this region is similar to the initial crystalline quality KDP has been measured at high pressure.[12] Phase V, believed to be orthorhombic, has a dielectric constant and volume discontinuity at the IV–V transition consistent with our observation. The 20–30 ns time delay in forming this phase is also consistent with a symmetry-changing transition.

In closing, we obtained time-sequenced images of ns time-scale morphological changes during single laser damage events. The images allow velocities and the competition between strain relief, deformation, and cracking to be viewed directly under divergent load. This technique can be extended to obtain more images per event at shorter time scales and applied to other material systems.

This work was performed under the auspices of the U.S. DOE through the UC-LLNL Institute for Laser Science and Applications under Contract No. W-7405-ENG-48.

[1] G. Tas, J. Franken, S. A. Hambir, D. E. Hare, and D. D. Dlott, Phys. Rev. Lett. **78**, 4585 (1997).
[2] J. Franken, S. A. Hambir, and D. D. Dlott, J. Appl. Phys. **85**, 2068 (1999).
[3] R. Evans, A. D. Badger, F. Fallies, M. Mahdieh, T. A. Hall, P. Audebert, J.-P. Geindre, J.-C. Gauthier, A. Mysyrowicz, G. Grillon, and A. Antonetti, Phys. Rev. Lett. **77**, 3359 (1996).
[4] J. F. Boudet and S. Ciliberto, Phys. Rev. Lett. **80**, 41 (1998).
[5] J. A. Hauch, D. Holland, M. P. Marder, and H. L. Swinney, Phys. Rev. Lett. **82**, 3823 (1999).
[6] C. V. Shank, R. Yen, and C. Hirlimann, Phys. Rev. Lett. **50**, 454 (1983); Phys. Rev. Lett. **51**, 900 (1983); B. J. Keay, M. Mendenhall, and G. S. Edwards, Phys. Rev. B **60**, 10898 (1999).
[7] A. Loveridge-Smith, A. Allen, J. Belak, T. Boehly, A. Hauer, B. Holian, D. Kalantar, G. Kyrala, R. W. Lee, P. Lombdahl, M. A. Meyers, D. Paisley, S. Pollaine, B. Remington, D. C. Swift, S. Weber, and J. S. Wark, Phys. Rev. Lett. **86**, 2349 (2001).
[8] J. S. Steckenrider and J. W. Wagner, Int. J. Fract. **73**, 213 (1995).
[9] N. Zaitseva, J. Atherton, R. Rozsa, L. Carman, I. Smolsky, M. Runkel, R. Ryon, and L. James, J. Cryst. Growth **197**, 911 (1999).
[10] J. J. De Yoreo and B. W. Woods, J. Appl. Phys. **73**, 7780 (1993).
[11] E. Rapoport, J. B. Clark, and P. W. Richter, J. Solid State Chem. **24**, 423 (1978).
[12] Y. Kobayashi, S. Endo, K. Koto, T. Kikegawa, and O. Shimomura, Phys. Rev. B **51**, 9302 (1995); Y. Kobayashi, S. Endo, K. Deguchi, O. Shimomura, and T. Kikegawa, Phys. Rev. B **55**, 2850 (1997).